THE JOURNAL OF PHYSICAL CHEMISTRY A

ARTICLE

pubs.acs.org/JPCA

# Imaging $H_2O$ Photofragments in the Predissociation of the HCl−$H_2O$ Hydrogen-Bonded Dimer

Blithe E. Rocher-Casterline, Andrew K. Mollner,† Lee C. Ch'ng, and Hanna Reisler*

Department of Chemistry, University of Southern California, Los Angeles, California 90089-0482, United States

Supporting Information

**ABSTRACT:** The state-to-state vibrational predissociation (VP) dynamics of the hydrogen-bonded HCl−$H_2O$ dimer was studied following excitation of the dimer's HCl stretch by detecting the $H_2O$ fragment. Velocity map imaging (VMI) and resonance-enhanced multiphoton ionization (REMPI) were used to determine pair-correlated product energy distributions. Following vibrational excitation of the HCl stretch of the dimer, $H_2O$ fragments were detected by 2 + 1 REMPI via the $\tilde{C}\ ^1B_1\ (000) \leftarrow \tilde{X}\ ^1A_1\ (000)$ transition. REMPI spectra clearly show $H_2O$ from dissociation produced in the ground vibrational state. The fragments' center-of-mass (c.m.) translational energy distributions were determined from images of selected rotational states of $H_2O$ and were converted to rotational state distributions of the HCl cofragment. The distributions were consistent with the previously measured dissociation energy of $D_0 = 1334 \pm 10\ cm^{-1}$ and show a clear preference for rotational levels in the HCl fragment that minimize translational energy release. The usefulness of 2 + 1 REMPI detection of water fragments is discussed.

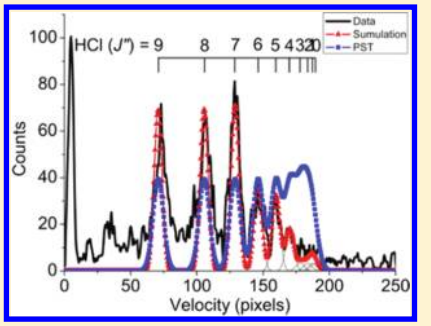


## 1. INTRODUCTION

Physical chemistry research has long sought to understand the nature, strength, and dynamics of hydrogen bonds. Hydrogen bonding plays an important role in a variety of chemical systems from gas-phase dimers to complex biological molecules. Experiments providing detailed state-specific information about the vibrational predissociation (VP) of small hydrogen-bonded complexes are needed to extend our understanding to larger systems and for testing the accuracy of calculated potential energy surfaces (PES). One of the experimental techniques that provide state-specific information on VP is photofragment velocity map imaging (VMI).[1−3] A limitation of the present method is that it requires that at least one photofragment be detected by resonance-enhanced multiphoton ionization (REMPI). This complicates, for example, the VP studies of pure $H_2O$ clusters because REMPI has not been used previously to detect $H_2O$ photofragments state-specifically.

HCl−$(H_2O)_x$ complexes have generated much interest because theory predicts that it takes only 4−5 water molecules for HCl to behave as an acid.[4−6] The state-to-state VP dynamics of the HCl−$H_2O$ dimer have been examined before using similar techniques by detecting the HCl fragment via REMPI following excitation of the dimer's HCl stretch fundamental.[3] In the previous study, $H_2O$ state distributions pair-correlated with individual HCl rotational states were derived from images obtained by detecting selected HCl ($J''$) levels. In this paper we present results of the first experiments in which $H_2O$ is detected by REMPI as a photofragment of VP. Directly detecting $H_2O$ fragments in VP of the HCl−$H_2O$ dimer provides the added benefit of observing HCl rotational distributions pair-correlated with specific water states, which is complementary to our previous study.[3]

From the perspective of developing a REMPI scheme for water products, detection of the $H_2O$ fragments provides an opportunity to examine $H_2O$ in states with higher rotational excitation, and the HCl−$H_2O$ dimer serves as a good test case for evaluating the feasibility of using the $H_2O$ 2 + 1 REMPI scheme. At the energy used to excite the HCl stretch fundamental of the dimer, vibrational excitation of HCl or $H_2O$ is energetically inaccessible, and the large rotational constant of the diatomic HCl fragment limits the number of its accessible rotational states to $J'' \leq 11$. This allows the pair-correlated rotational states of the HCl fragment to be determined unambiguously from $H_2O$ images.

The Rydberg states of $H_2O$ have been studied extensively via multiphoton spectroscopy at room temperature and in molecular beams. The $\tilde{C}\ ^1B_1 \leftarrow \tilde{X}\ ^1A_1$ transition has been investigated previously by 3 + 1 REMPI detection,[7,8] and more recently 2 + 1 REMPI spectroscopy was used to investigate several Rydberg states.[9−12] Both schemes have been successfully implemented for detection of $H_2O$ in molecular beams,[8−10] and in scattering experiments.[13,14]

One known complication of $H_2O$ detection via REMPI is the predissociation of high rotational levels of the $\tilde{C}$-state. Both heterogeneous and homogeneous predissociation have been observed, with predissociation being the dominant lifetime-broadening factor.[7,8,11,12,15] The heterogeneous predissociation

**Special Issue:** J. Peter Toennies Festschrift

**Received:** December 17, 2010
**Revised:** February 13, 2011
**Published:** March 09, 2011

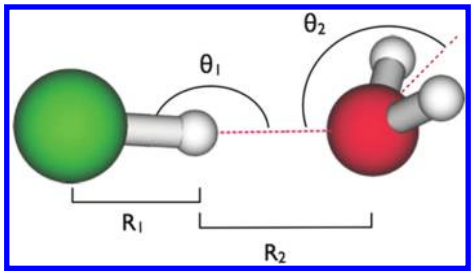


**Figure 1.** Minimum energy geometry of the HCl−$H_2O$ dimer.[17] $\theta_1$ = 178.4°; $\theta_2$ = 133.7°; $R_1$ = 1.287 Å; $R_2$ = 1.933 Å.

lifetime has a strong dependence on the component of the rotation along the *a*-axis, and it takes place most likely via the $\tilde{B}\ ^1A_1$ state. The homogeneous predissociation mechanism is independent of rotational level, and dissociation is via the $\tilde{A}\ ^1B_1$ state.[7] The most recent study by Yang et al. reports a significantly narrower linewidth ($\geq$1.3 $cm^{-1}$, attributed to homogeneous predissociation) than in previous studies indicating a longer lifetime of the $\tilde{C}$-state.[12]

In the study of Yang et al.,[12] only lower energy rotational states ($J'' = 0-3$) of the ground electronic state of water were detected. In the present work, $H_2O$ states with higher rotational excitation ($J'' \leq 11$) are expected to be populated. Yang et al. also provide rotational parameters that can be used in a standard simulation program (PGOPHER)[16] to simulate the $H_2O$ REMPI spectrum. The simulation used by Yang et al. included a linewidth model that accounted for lifetime broadening due to predissociation of the excited state.[12]

Referring to the state-to-state VP of the HCl−$H_2O$ dimer, the structure of the dimer has been studied previously both experimentally and theoretically.[17−20] The minimum energy structure is shown in Figure 1. The dimer has a nearly linear hydrogen bond ($\angle$OHCl $\approx$ 178°), with the HCl acting as a hydrogen bond donor to the oxygen of water. The calculated global minimum structure[17] ($\theta_2$ = 133.7°) in Figure 1 differs from the experimentally determined equilibrium geometry[18,19] ($\theta_2$ = 145.3°) due to averaging over all experimentally observed angles.

Complexes were formed in a pulsed molecular beam, and the dimer's HCl stretch fundamental was excited by a pulsed IR laser to induce predissociation. Individual $H_2O$ ($J''_{KaKc}$) rotational states were selected by 2 + 1 REMPI and VMI was used to measure the pair-correlated HCl distributions for selected $H_2O$ states. While the congested and predissociative $H_2O$ REMPI spectrum limits the states that can be used for imaging, we demonstrate that it is possible to measure some pair-correlated HCl distributions by VMI. These distributions are consistent with the previously measured dissociation energy of $D_0$ = 1334 ± 10 $cm^{-1}$ and show a clear preference for the formation of high rotational states of the HCl cofragment that minimize translational energy release.

## 2. EXPERIMENTAL DETAILS

VP of HCl−$H_2O$ formed in a pulsed supersonic molecular beam was studied following pulsed IR laser excitation. Rotationally excited $H_2O$ fragments were ionized by 2 + 1 REMPI and detected by time-of-flight (TOF) mass spectrometry and VMI. The experimental procedures were similar to those used in our previous studies.[3,21−24]

The dimers were formed in a pulsed supersonic molecular beam by expanding a mixture of 0.5% $H_2O$ and 3% HCl (Matheson Trigas, 99.995%) in He (Gilmore, 99.999%) at a stagnation pressure of ~ 2 atm through the 0.5-mm orifice of a pulsed valve (~ 150 $\mu$s opening time) operating at 10 Hz. Samples were prepared by transferring $H_2O$ by vacuum distillation to an evacuated bulb followed by adding gaseous HCl. The backing pressure and concentrations were optimized to maximize the signal from the dimer. The skimmed molecular beam was intersected at right angles by two counter-propagating laser beams in the interaction region. Focused IR laser radiation (1.0−6.5 mJ/pulse, lens focal length (f.l.) = 50 cm, ~ 0.4 $cm^{-1}$ linewidth) was used to excite the HCl stretch of the dimer at 2723 $cm^{-1}$. The IR radiation was generated by an optical parametric oscillator/amplifier (OPO/OPA) system (LaserVision) pumped by the fundamental of a seeded Nd:YAG laser (Continuum Powerlite 8000). The IR frequency was calibrated by measuring the well-known absorption spectrum of gaseous HCl.

Focused ultraviolet (UV) radiation (0.2 − 1.1 mJ/pulse, f. l. = 20 cm; ~ 0.4 $cm^{-1}$ linewidth) was used to ionize $H_2O$ fragments state-selectively. For imaging, the UV beam was expanded by using an additional lens (f.l. = −100 cm) placed 86 cm before the focusing (f.l. = 20 cm) lens. The addition of the negative focal length lens expanded the laser beam prior to focusing to provide tighter focusing and a higher photon density to increase the ionization efficiency of the $H_2O$ fragment. Attempts were made to focus even more tightly, but a signal likely due to multiphoton absorption and/or weak overlapping transitions became observable, interfering with single state selection. As an alternative, utilizing a tunable picosecond laser would increase the pumping rate and maximize the efficiency of $H_2O$ detection by competing more effectively with dissociation.

UV radiation at 247−250 nm was generated by frequency-doubling (Inrad Autotracker III) the output of a dye laser (Continuum ND 6000, Coumarin 500) pumped by a Nd:YAG laser (Continuum SureliteIII) and frequency calibrated by the known REMPI spectrum of HCl. The $\tilde{C}\ ^1B_1$ (000) ← $\tilde{X}\ ^1A_1$ (000) transition was used for $H_2O$ photofragment detection. The UV spectra were modeled using the program PGOPHER[16] with rotational constants from Yang et al. as discussed below.[12] Background signals due to room temperature $H_2O$ monomers were reduced by modifying the chamber design to include a cryopumping system cooled by several liquid nitrogen traps.

The timing of the lasers was adjusted by a delay generator (Stanford, DG535) controlled through a GPIB interface (National Instruments). Spectra were collected by alternating "IR on" and "IR off" conditions at each frequency. In "IR on", the IR laser was fired 70 ns before the UV laser, whereas in "IR off", the IR laser was fired 2 $\mu$s after the UV laser. Laser conditions (timing, focusing, power) were optimized to maximize signal from the dimer while ensuring that no contributions from other $H_2O$-containing clusters were observed. The timing of the lasers' firings was carefully optimized to excite dimers in the coldest part of the molecular beam pulse where their highest relative abundance was found.

The VMI arrangement has been described in detail previously.[1,2] In brief, it consists of a four-electrode ion acceleration assembly, a 60-cm field-free drift tube, and a microchannel plate (MCP) detector (BURLE Electro-Optics Co.) coupled to a phosphor screen that is monitored by a charge-coupled device (CCD) camera (LaVision, Imager). In this experiment, two modes were used to collect data: (i) TOF mass spectrometry for spectroscopic investigations and (ii) VMI mode for determining center-of-mass (c.m.)

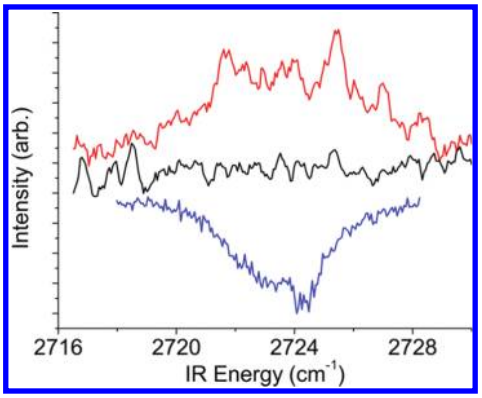


**Figure 2.** Fragment yield IR spectra of the dimer. The red (top) line shows the spectrum assigned to HCl−$H_2O$ taken while monitoring the $H_2O$ photofragment with 1.0 mJ IR pulse energy (f.l. = 50 cm), in a mixture of 0.5% $H_2O$, 3% HCl, and 2 atm backing pressure. The black (middle) line shows the background signal from $H_2O$ monomers in the molecular beam under the same conditions. The blue (bottom) line shows the previously published[3] IR enhancement spectrum taken while monitoring the HCl photofragment with 1.5 mJ IR pulse energy (unfocused), 1% $H_2O$, 3% HCl, and 1 atm backing pressure. Both IR and UV laser powers were held constant over the range of the scan.

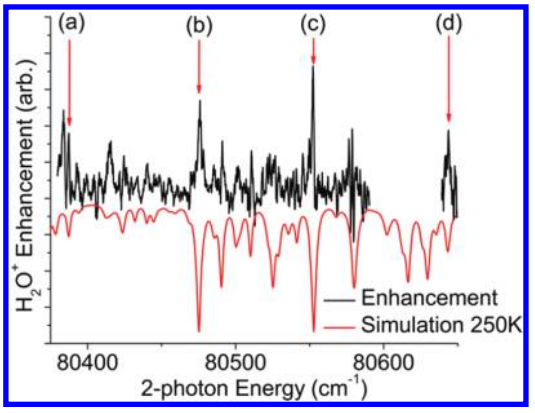


**Figure 3.** The black (top) line corresponds to the $H_2O$ photofragment 2 + 1 REMPI enhancement spectrum obtained by exciting the HCl stretch of HCl−$H_2O$ at 2723 cm$^{-1}$ and scanning the UV laser through the region of the $\tilde{C}\,^1B_1$ (000) ← $\tilde{X}\,^1A_1$ (000) transition of $H_2O$. The red (bottom) line corresponds to the simulated spectrum at $T$ = 250 K. The labeled transitions are dominated by (a) $2_{02} \leftarrow 4_{23}$, (b) $2_{02} \leftarrow 3_{21}$, (c) $2_{02} \leftarrow 2_{21}$, and (d) $4_{13} \leftarrow 4_{14}$. Note: the intensity of the peak labeled "d" is not normalized to the other peaks because it had to be recorded separately. The gap in the data corresponds to the region of low-$J$ transitions for which the background intensity was too large to measure enhancement. Both IR and UV laser powers were held constant over the range of the scan.

translational energy distributions. In VMI mode, the two-dimensional projections were collected using an event counting method (DaVis) and reconstructed to three-dimensional images using the BASEX method.[25] Speed distributions were obtained by summing over the angular distribution for each radius, and were converted to c.m. translational energy distributions using momentum conservation, the appropriate Jacobian, ($\propto E_T^{-1/2}$), and calibration constants obtained by imaging O products from the well-known $O_2$ photodissociation.[26] The translational energy distributions were analyzed to determine the internal energy distributions of the HCl cofragments as well as the dissociation threshold of HCl−$H_2O$.

The $H_2O$ ($J''_{KaKc}$) fragments that can be detected state-selectively by the 2 + 1 REMPI are limited by the lifetimes of the excited states, the selection rules, and spectral overlap of the transitions. A PGOPHER simulation that also takes into account lifetime broadening effects due to predissociation of the excited state was used previously by Yang et al.[12,14] The predissociation rate scales with $\langle J_a^2 \rangle$, the average of the square of the operator for the projection of $J'$ onto the $a$-axis. It should be noted that $K_a'$ is in fact not a good quantum number for asymmetric tops, therefore $\langle J_a^2 \rangle$ is used in ref 9 instead of $\langle K_a^2 \rangle$. Here we follow the commonly used $J''_{KaKc}$ notation for clarity. The simulation only includes the $\tilde{C}\,^1B_1$ (000) ← $\tilde{X}\,^1A_1$ (000) origin band and it fits the spectral line positions well. For convenience, a summary of the relevant selection rules for two-photon absorption[27] is presented in the Appendix.

## 3. RESULTS AND DISCUSSION

**3.1. Infrared Action Spectra.** IR action spectra of the dimer in the frequency region of the HCl stretch fundamental were obtained by monitoring $H_2O$ photofragments by REMPI while scanning the IR laser frequency. A typical spectrum recorded at 2716−2732 cm$^{-1}$ by monitoring a group of overlapping states dominated by $H_2O$ ($J''_{KaKc}$ = $3_{21}$) is shown in Figure 2 and compared with the previously published[3] IR spectrum of the dimer taken by monitoring HCl photofragments. The spectral curve depicts the enhancement of the $H_2O^+$ signal following IR excitation. The background $H_2O^+$ signal taken with the IR laser off is also shown. It is important to note that these are action spectra; in order to observe enhancement, there must be absorption of IR photons, and this absorption must lead to the production of $H_2O$ fragments in the monitored $J''_{KaKc}$ state. No contributions from other $H_2O$-containing clusters were seen in the region of the dimer peak (2709−2738 cm$^{-1}$). The spectrum shown in Figure 2 exhibits saturation broadening due to the tight focusing conditions necessary to maximize the signals from the $H_2O$ fragments.

The position of the HCl-stretch band in the HCl−$H_2O$ dimer shown in Figure 2 is in good agreement with the previously reported spectra.[3,18,28,29] The high-frequency and low-frequency peaks in the action spectra obtained by monitoring the $H_2O$ fragments are less well resolved than spectra recorded previously by monitoring HCl fragments. This is likely due to the higher IR laser power and tighter focusing conditions required to detect $H_2O$ fragments. Because we compare action spectra, we note that the observed IR intensities are proportional to both the absorption cross section at the excitation frequencies and the fractional yield of the monitored HCl ($J''$) or $H_2O$ ($J''_{KaKc}$) fragment states. The lower signal-to-noise ratio in the $H_2O$ ($J''_{KaKc}$) spectrum relative to HCl ($J''$) is a result of the lower REMPI efficiency and greater number of fragment quantum states of $H_2O$. The similarity of the two spectra and the absence of absorption bands from larger clusters near the dimer band confirm that the $H_2O$ ($J''_{KaKc}$) signals observed by monitoring $H_2O$ derive from VP of the HCl−$H_2O$ dimer.

**3.2. REMPI Spectroscopy of Water Fragments.** A representative REMPI spectrum of $H_2O$ fragments in the region of the $\tilde{C}\,^1B_1$ (000) ← $\tilde{X}\,^1A_1$ (000) transition obtained following 2723 cm$^{-1}$ excitation of HCl−$H_2O$ is shown in Figure 3. The spectrum shows enhancement (relative to the IR off signal) for several states that can be used for imaging. A simulation with a rotational temperature of 250 K is also shown for comparison of

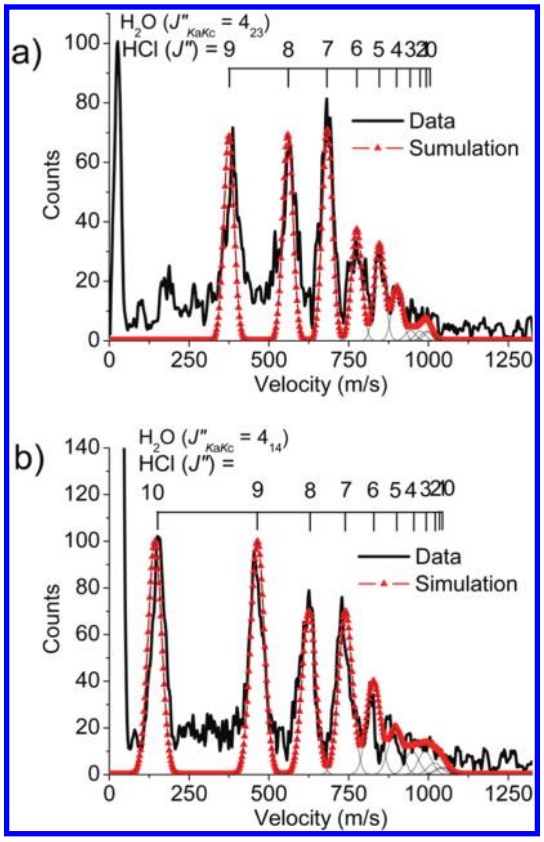


**Figure 4.** The black (solid) line corresponds to the BASEX-reconstructed image of state-selected $H_2O$ fragments (a) ($J''_{KaKc} = 4_{23}$) and (b) ($J''_{KaKc} = 4_{14}$) produced in the VP of HCl−$H_2O$ plotted as a velocity distribution in units of m/s (velocity in m/*s* = 5.3 × pixels). The red (triangles) line corresponds to the total simulated fit of the image. The Gaussians are labeled with the corresponding rotational levels of the HCl cofragment. The images were collected over approximately (a) 400 000 shots with 0.4 mJ UV pulse energy and (b) 230 000 shots with 0.9 mJ UV pulse energy.

line positions. The simulation uses the published rotational constants and the PGOPHER[16] program from Yang et al.[12] State-selection of $H_2O$ ($J''_{KaKc}$) levels was complicated by the fast predissociation in the $\tilde{C}$-state for many states as well as spectral congestion and overlap. Background signals from ambient $H_2O$ monomers were reduced by a factor of 5 by using several liquid nitrogen cooled traps. The background REMPI spectrum was fit well with $T$ = 300 K. The most intense enhancements originated from overlapping transitions dominated by $H_2O$ ($J''_{KaKc} = 3_{21}$) and $H_2O$ ($J''_{KaKc} = 2_{21}$) as seen in Figure 3. The only transitions in this study that were identified as isolated from other transitions *and* showed significant enhancement following VP were those with $H_2O$ ($J''_{KaKc} = 4_{23}$) and $H_2O$ ($J''_{KaKc} = 4_{14}$).

**3.3. Ion Imaging Results and Analysis.** Representative velocity spectra obtained by VMI are shown in Figure 4a for $H_2O$ ($J''_{KaKc} = 4_{23}$) and Figure 4b for $H_2O$ ($J''_{KaKc} = 4_{14}$), as the BASEX reconstruction of the raw images plotted in velocity space (m/s). All observed angular distributions of the images were isotropic. The size of the image in pixels is the radial distance from the center of the image and is proportional to the speed of the $H_2O^+$ fragment. The speed (m/s) is equal to 5.3 times the number of pixels. The UV power and focusing conditions were optimized for the best signal-to-noise ratio for each image. Higher UV fluence, obtained either by increasing the UV power or placing the negative lens further from the focusing lens (see Section 2) to provide tighter focusing, resulted in unresolved peaks due to power broadening and/or background contributions. For the $J''_{KaKc} = 4_{23}$ and $3_{21}$ images, a lower UV fluence (0.4 mJ/pulse, f.l. = −100 cm lens placed 86 cm before f.l. = 20 cm lens) was used to minimize contributions from neighboring transitions. A higher UV fluence (0.9 mJ/pulse) was used for the $J''_{KaKc} = 4_{14}$ image, as this transition is well isolated and no background contributions were observed even at high fluences.

Reconstructed images in velocity space were used to determine the rotational state populations of pair-correlated HCl fragments. Fitting in velocity space instead of energy space improves our ability to resolve structures at low $E_T$ and identify the maximum observed $E_T$. Fitting was accomplished by assigning a Gaussian-shaped curve to each rotational state of HCl with a width characteristic of our experimental resolution (full width at half-maximum (fwhm) ∼ 8 pixels). The positions of these Gaussians were determined by using the known dissociation energy of the HCl-$H_2O$ dimer, $D_0$ = 1334 cm$^{-1}$,[3] and conservation of energy. The heights of the Gaussians were first described by a smooth function of $E_T$ and then, when resolved, were adjusted to fit distinct features of the image.

The speed distributions were converted to c.m. translational energy distributions as described in section 2. Using the excitation energy and $D_0$ we obtain $h\nu - D_0$ = 2723 − 1334 = 1389 cm$^{-1}$. Therefore, vibrational modes of neither monomer are energetically accessible and $E_{vib}$(HCl) and $E_{vib}$($H_2O$) are set to zero, resulting in

$$E_{int}(\mathrm{HCl{-}H_2O}) + h\nu = D_0 + E_T + E_{rot}(\mathrm{HCl}) + E_{rot}(\mathrm{H_2O})$$

where $E_{int}$(HCl−$H_2O$) is the internal energy of the dimer prior to excitation, $h\nu$ is the photon energy used for vibrational excitation of the dimer (2723 cm$^{-1}$), $E_T$ is the c.m. translational energy, and $E_{rot}$(HCl) and $E_{rot}$($H_2O$) are the rotational energies of the HCl and $H_2O$ fragments, respectively. The internal energy of the dimer, $E_{int}$(HCl−$H_2O$), is estimated to be 1 ± 1 cm$^{-1}$ from the $T$ = 5 K Boltzmann distribution in the molecular beam with mainly HCl−$H_2O$ ($J''$ = 1 and 2) states populated. State selection in the REMPI detection defines $E_{rot}$($H_2O$), and $E_T$ is determined from the images. Rotational states of HCl are assigned by fitting the structure in the images to the known rotational energies of HCl. This procedure establishes that the highest allowed rotational states of HCl are populated preferentially for each imaged $H_2O$ ($J''_{KaKc}$) fragment.

One disadvantage of obtaining images by detecting $H_2O$ fragments by REMPI is the difficulty of finding isolated transitions. When the $H_2O$ transition is not overlapped with other transitions, the structure in the image corresponding to HCl rotational states can be assigned unambiguously, and an accurate value of $D_0$ can be determined. As in previous cases,[3,21−24] all images with clearly observable structure could be fit accurately with a unique value of $D_0$. By contrast, most of the transitions in the REMPI spectrum of water are overlapped. When a rotational state with low $K_a'$ overlaps transitions with rotational states with high $K_a'$, the transitions with high $K_a'$ can usually be neglected in the image fitting because they are broadened much more by fast predissociation and contribute less to the peak height in the REMPI spectrum.

The $H_2O$ distributions shown in Figure 4 were fit with the previously published value of $D_0$ for the HCl−$H_2O$ dimer.[3] For

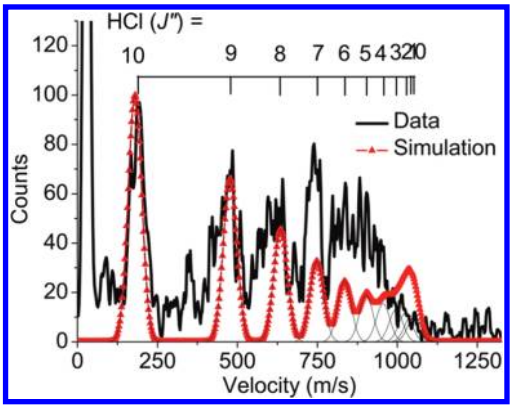


**Figure 5.** The black (solid) line corresponds to the BASEX-reconstructed image of $H_2O$ fragments produced in the VP of HCl−$H_2O$ plotted as a velocity distribution in units of m/s (velocity in m/$s$ = 5.3 × pixels). The image is dominated by the $H_2O$ $2_{02} \leftarrow 3_{21}$ transition, although it likely has contributions from several other overlapped transitions. The red (triangles) line corresponds to a simulation of line positions assuming $H_2O$ ($J''_{KaKc} = 3_{21}$). The Gaussians are labeled with the corresponding rotational levels of the HCl cofragment. The heights of the Gaussians are described by a smooth function of $E_T$ and are normalized to the peak height of HCl ($J'' = 10$). The image was collected over approximately 610 000 shots with 0.4 mJ UV pulse energy.

these $H_2O$ states, most of the individual HCl rotational states are clearly resolved, and the fits are unambiguous. When images were recorded by monitoring overlapped transitions of $H_2O$, some rotational structure could still be resolved for the HCl cofragment, and images were consistently fit with $D_0$ = 1334 $cm^{-1}$, even though a unique pair-correlated HCl distribution could not be determined. An example is shown in Figure 5. Several features in the image could not be fit without including the $H_2O$ $2_{02} \leftarrow 3_{21}$ transition in the simulation. Although the image could be better fit by including, for example, the nearby $5_{05} \leftarrow 6_{06}$, $5_{15} \leftarrow 6_{16}$, and/or $4_{23} \leftarrow 5_{24}$ transitions, the fitting was not unique, and we could not conclusively determine which one(s) contribute(s) to the image. In addition, it is possible that other broad transitions, whose peaks are farther away, also contribute to the image. Because all of the contributing $H_2O$ states could not be determined for this image, the heights of the Gaussians pair-correlated with $H_2O$ ($J''_{KaKc} = 3_{21}$), were described by a smooth function of $E_T$ and not adjusted to fit the heights of distinct structural features in the image. Although the relative populations of the HCl states could not be unambiguously determined from the image, $D_0$ could be estimated even when monitoring an overlapped transition of $H_2O$.

**3.4. Fragments' Translational and Rotational Energy Populations.** The imaging data provide information on the relative populations of the rotational states of the HCl cofragment pair-correlated with specific $H_2O$ ($J''_{KaKc}$) states. Only a modest number of rotational states of HCl ($J'' \leq 11$) are energetically allowed, whereas a larger number of $H_2O$ ($J''_{KaKc}$) levels can be energetically populated. The rotational distributions of the HCl cofragment pair-correlated with specific rotational states of $H_2O$ encompass all of the $J''$ levels allowed by energy conservation. For example, in the c.m. $E_T$ distribution for $J''_{KaKc} = 4_{23}$ shown in Figure 6a, where $h\nu$ = 2723 $cm^{-1}$, and $E_{rot}(H_2O)$ = 300 $cm^{-1}$, the energy available for c.m. translation or rotation of the HCl fragment is ~1090 $cm^{-1}$. Thus, only HCl ($J'' \leq 9$) states can be populated. The observed pair-correlated HCl rotational states are consistent with this prediction, and the maximum translational energy is consistent with the published value of $D_0$.

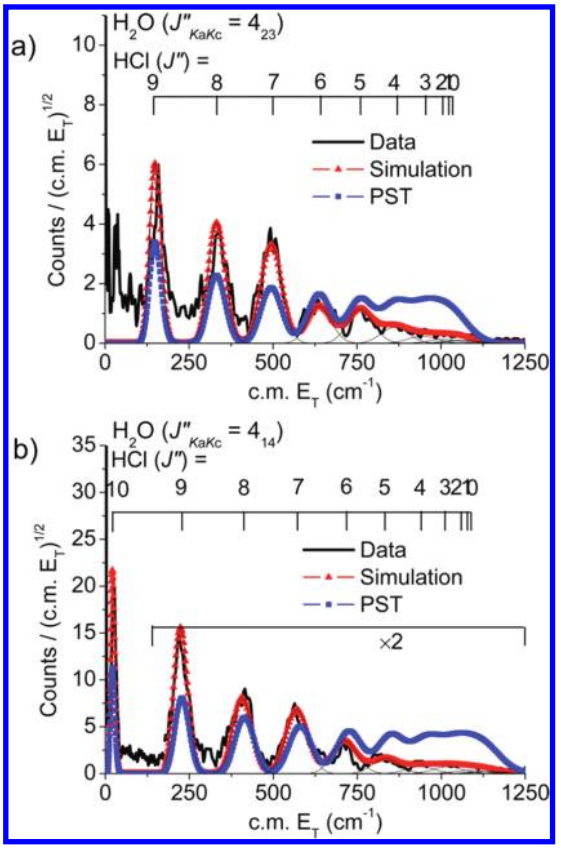


**Figure 6.** Translational energy distributions derived from the reconstructed images shown in Figure 4. The black (solid) lines correspond to the images of state-selected $H_2O$ fragments (a) ($J''_{KaKc} = 4_{23}$) and (b) ($J''_{KaKc} = 4_{14}$) of HCl−$H_2O$. The red (triangles) lines correspond to the total simulated fits of the images. The Gaussians are labeled with the corresponding rotational levels of the HCl cofragment. The blue (squares) lines correspond to translational energy distributions calculated by PST. The areas under the PST plots are normalized to the areas under the simulation plots.

We can compare the observed pair-correlated distributions with the prediction of statistical theories. Previously we were unable to determine whether the HCl rotational state distribution was statistical because the populations of several rotational levels could not be determined due to experimental difficulties.[3] The observed HCl populations appeared evenly distributed among all accessible rotational states. On the other hand, we showed that the high water rotational states pair-correlated with each HCl ($J''$) state were favored relative to the statistical predictions (phase space theory (PST)). Due to conservation of energy, these states must be paired with low rotational levels of HCl. This in effect causes a more even distribution of HCl rotational state populations when all $H_2O$ rotational states are taken into account. By imaging a single rotational state of $H_2O$, we are able to compare the pair-correlated HCl rotational state distribution for each $H_2O$ rotational state with statistical calculations.

Figure 6 demonstrates that the rotational energy distributions of HCl fragments pair-correlated with a specific $H_2O$ ($J''_{KaKc}$) state are nonstatistical, with HCl fragments that have the highest allowed rotational energy (low $E_T$) more highly populated than predicted by PST.[3,30−33] Accordingly, fragments with low rotational energy (high $E_T$) are less populated than predicted by PST.

The individual rotational populations used in the fits and statistical calculations are listed in the Supporting Information, but the trend is clearly visible in Figure 6.

The results on rotational excitation agree well with the propensity rules described by Ewing,[34−36] which combine the momentum (or energy) gap law with the requirement that the number of quanta transferred in the VP be minimized. This model explains why the preferred VP route often involves small translational energy ($E_T$) release, i.e., high rotational excitation when no excited vibrational levels are available. The complementary angular momentum (AM) model proposed by McCaffery and co-workers[37,38] is based on linear-to-angular momentum interconversion. It has been used recently to describe rotational distributions in the VP of weakly bound dimers. Realizing that there is insufficient anisotropy in the long-range part of the PES to explain the observed high fragement rotational excitation, the involvement of the repulsive, hard-shaped part of the PES is invoked. The AM model identifies the principal geometries and impact parameters from which dissociation occurs and reproduces well the fragments' rotational distributions. The results suggest that the extent of rotational excitation is constrained by the hard-shaped potential, dimer geometry, and angular momentum conservation. Using these considerations, it was possible to predict some fragment HX rotational excitation in a series of acetylene−HX dimers (X = F, Cl, O) excited to the HX or asym-CH stretch vibration.[39] The nonstatistical nature of most of the observed rotational distributions in HX-containing complexes suggests that interactions with the repulsive part of the potential are more important than initial coupling of the OH stretch to all the available intermolecular modes followed by statistical predissociation.

## 4. SUMMARY AND CONCLUSIONS

The state-to-state VP of the hydrogen-bonded HCl−$H_2O$ dimer was studied following excitation of the bound HCl stretch via detection of the $H_2O$ photofragment. VMI and REMPI were used to determine the product energy distributions. Following vibrational excitation of the bound HCl stretch fundamental, $H_2O$ fragments were detected by 2 + 1 REMPI via the $\tilde{C}\ ^1B_1$ (000) ← $\tilde{X}\ ^1A_1$ (000) transition. The fragments' c.m. translational energy distributions were determined from images of selected rotational states of $H_2O$ and were converted to rotational state distributions of the HCl cofragment. All the distributions could be fit well when using the previously published dissociation energy of $D_0$ = 1334 $cm^{-1}$. The rotational energy distributions of the HCl cofragment pair-correlated with specific rotational states of $H_2O$ encompassed all of the $J''$ levels allowed by energy conservation. A detailed analysis of pair-correlated state distributions was complicated by the $H_2O$ REMPI spectrum, but the results show that the HCl rotational populations are nonstatistical with preference to rotational states that minimize translational energy release, in agreement with the conclusions reached from images of HCl ($J''$) fragments.

In addition, the HCl−$H_2O$ dimer study proves the feasibility of using the $H_2O$ 2 + 1 REMPI scheme to detect $H_2O$ fragments, even when water is a minor species of the sample. Compared to detection of $NH_3$ and HCl fragments,[3,21] $H_2O$ detection suffers from severe band overlap in the $\tilde{C}\ ^1B_1$ (000) ← $\tilde{X}\ ^1A_1$ (000) transition, which makes selection of isolated $H_2O$ states difficult. Additionally, the upper state is predissociative, reducing the REMPI efficiency, and only transitions with upper states having low values for $K_a'$ can be detected. While the signal is reduced relative to monitoring the HCl and $NH_3$ fragments, the achieved signal-to-noise ratio in the images is sufficient to determine both $D_0$ and the pair-correlated state distributions. In the future, it may be advantageous to look for REMPI systems other than the $\tilde{C}\ ^1B_1$ (000) ← $\tilde{X}\ ^1A_1$ (000) transition for $H_2O$ detection, and to use a picosecond laser to compete effectively with predissociation. The successful detection and imaging of the $H_2O$ fragment provides a basis for looking at larger, more complicated $H_2O$-containing complexes, including the $H_2O$−$H_2O$ dimer.

## APPENDIX

The selection rules for two-photon absorption are analogous to vibrational Raman selection rules.[27] The general selection rules for rovibrational Raman transitions of asymmetric rotors such as the $H_2O$ molecule with $C_{2v}$ symmetry are

$$\Delta J = 0, \pm 1, \pm 2 \text{ for } (J'' + J') \geq 2$$

$$\Delta K_a = 0, \pm 1, \pm 2$$

$$\Delta K_c = 0, \pm 1, \pm 2$$

In addition, the product of the symmetry species of the upper and lower rovibronic states, $\Gamma(\psi'_{rve})$ and $\Gamma(\psi''_{rve})$, respectively, and the elements of the two-photon transition tensor, **S**, must be fully symmetric for a rovibronic transition to be allowed.

$$\Gamma(\psi'_{rve}) \otimes \Gamma(S_{ij}) \otimes \Gamma(\psi''_{rve}) \supset A_1$$

Selection rules involving the parity, i.e. the evenness or oddness of $K_a$ and $K_c$, also depend on the direction of the permanent dipole moment in the molecule. The vibronic symmetry species of the $\tilde{C}\ ^1B_1$ (000) state is $b_1$ and the vibronic symmetry species of the $\tilde{X}\ ^1A_1$ (000) is $a_1$. Based on the selection rules for the $\tilde{C}\ ^1B_1$ (000) ← $\tilde{X}\ ^1A_1$ (000) transition, only rotational transitions with $b_1$ symmetry are allowed ($b_1 \otimes b_1 = a_1$) where the parity of $K_c$ changes as eo ↔ ee and oo ↔ oe, and where eo indicates that $K_a$ is even and $K_c$ is odd. All transitions observed meet these selection rule requirements.

## ASSOCIATED CONTENT

**Supporting Information.** A list of the individual rotational populations used in the fits and from the PST calculations is provided. This material is available free of charge via the Internet at http://pubs.acs.org.

## AUTHOR INFORMATION

### Corresponding Author

*E-mail: reisler@usc.edu. Ph: 213-740-7071. Fax: 213-740-3972.

### Present Addresses

†Aerospace Corporation, 2310 E. El Segundo Blvd., El Segundo, CA 90245, United States.

## ACKNOWLEDGMENT

This work was supported by the U.S. National Science Foundation. The authors would like to thank Professor Anthony McCaffery for stimulating discussions on the VP mechanism, Professor Colin Western for assistance with simulating the water REMPI spectra, and Professor David Parker for sharing results prior to publication.

## REFERENCES


(1) Eppink, A. T. J. B.; Parker, D. H. *Rev. Sci. Instrum.* **1997**, *68*, 3477.
(2) Dribinski, V.; Potter, A. B.; Fedorov, I.; Reisler, H. *J. Chem. Phys.* **2004**, *121*, 12353.
(3) Casterline, B. E.; Mollner, A. K.; Ch'ng, L. C.; Reisler, H. *J. Phys. Chem. A* **2010**, *114*, 9774.
(4) Lee, C. T.; Sosa, C.; Planas, M.; Novoa, J. J. *J. Chem. Phys.* **1996**, *104*, 7081.
(5) Milet, A.; Struniewicz, C.; Moszynski, R.; Wormer, P. E. S. *J. Chem. Phys.* **2001**, *115*, 349.
(6) Chaban, G. M.; Gerber, R. B.; Janda, K. C. *J. Phys. Chem. A* **2001**, *105*, 8323.
(7) Ashfold, M. N. R.; Bayley, J. M.; Dixon, R. N. *Chem. Phys.* **1984**, *84*, 35.
(8) Kuge, H. H.; Kleinermanns, K. *J. Chem. Phys.* **1989**, *90*, 46.
(9) Uselman, B. W.; Boyle, J. M.; Anderson, S. L. *Chem. Phys. Lett.* **2007**, *440*, 171.
(10) Dickinson, H.; Mackenzie, S.; Softley, T. *Phys. Chem. Chem. Phys.* **2000**, *2*, 4669.
(11) Meijer, G.; Termeulen, J. J.; Andresen, P.; Bath, A. *J. Chem. Phys.* **1986**, *85*, 6914.
(12) Yang, C.-H.; Sarma, G.; ter Meulen, J. J.; Parker, D. H.; Western, C. M. *Phys. Chem. Chem. Phys.* **2010**, *12*, 13983.
(13) Hama, T.; Yokoyama, M.; Yabushita, A.; Kawasaki, M.; Andersson, S.; Western, C. M.; Ashfold, M. N. R.; Dixon, R. N.; Watanabe, N. *J. Chem. Phys.* **2010**, *132*, 164508.
(14) Yang, C.; Sarma, G.; ter Meulen, J. J.; Parker, D. H.; Buck, U.; Wiesenfeld, L. *J. Phys. Chem. A* **2010**, *114*, 9886.
(15) Yuan, K.; Cheng, Y.; Cheng, L.; Guo, Q.; Dai, D.; Wang, X.; Yang, X.; Dixon, R. N. *Proc. Natl. Acad. Sci. U.S.A.* **2008**, *105*, 19148.
(16) Western, C. M. *PGOPHER, A Program for Simulating Rotational Structure*; University of Bristol: Bristol, U.K., 2010.
(17) Alikhani, M. E.; Silvi, B. *Phys. Chem. Chem. Phys.* **2003**, *5*, 2494.
(18) Huneycutt, A. J.; Stickland, R. J.; Hellberg, F.; Saykally, R. J. *J. Chem. Phys.* **2003**, *118*, 1221.
(19) Kisiel, Z.; Pietrewicz, B. A.; Fowler, P. W.; Legon, A. C.; Steiner, E. *J. Phys. Chem. A* **2000**, *104*, 6970.
(20) Legon, A. C.; Willoughby, L. C. *Chem. Phys. Lett.* **1983**, *95*, 449.
(21) Mollner, A. K.; Casterline, B. E.; Ch'ng, L. C.; Reisler, H. *J. Phys. Chem. A* **2009**, *113*, 10174.
(22) Li, G.; Parr, J.; Fedorov, I.; Reisler, H. *Phys. Chem. Chem. Phys.* **2006**, *8*, 2915.
(23) Pritchard, M.; Parr, J.; Li, G.; Reisler, H.; McCaffery, A. J. *Phys. Chem. Chem. Phys.* **2007**, *9*, 6241.
(24) Parr, J. A.; Li, G.; Fedorov, I.; McCaffery, A. J.; Reisler, H. *J. Phys. Chem. A* **2007**, *111*, 7589.
(25) Dribinski, V.; Ossadtchi, A.; Mandelshtam, V. A.; Reisler, H. *Rev. Sci. Instrum.* **2002**, *73*, 2634.
(26) Parker, D. H.; Eppink, A. T. J. B. *J. Chem. Phys.* **1997**, *107*, 2357.
(27) Hollas, J. M. *High Resolution Spectroscopy*, 2nd ed.; John Wiley & Sons, Ltd.: West Sussex, England, 1998.
(28) Farnik, M.; Weimann, M.; Suhm, M. A. *J. Chem. Phys.* **2003**, *118*, 10120.
(29) Weimann, M.; Farnik, M.; Suhm, M. A. *Phys. Chem. Chem. Phys.* **2002**, *4*, 3933.
(30) Pechukas, P.; Light, J. C. *J. Chem. Phys.* **1965**, *42*, 3281.
(31) Zyrianov, M.; Sanov, A.; Droz-Georget, T.; Reisler, H. *J. Chem. Phys.* **1999**, *110*, 10774.
(32) Potter, A. B.; Dribinski, V.; Demyanenko, A. V.; Reisler, H. *J. Chem. Phys.* **2003**, *119*, 7197.
(33) Baer, T.; Hase, W. L. *Unimolecular Reaction Dynamics: Theory and Experiments*; Oxford University Press: New York, 1996.
(34) Ewing, G. E. *J. Phys. Chem.* **1987**, *91*, 4662.
(35) Ewing, G. E. *J. Chem. Phys.* **1980**, *72*, 2096.
(36) Ewing, G. E. *J. Chem. Phys.* **1979**, *71*, 3143.
(37) Osborne, M. A.; McCaffery, A. J. *J. Chem. Phys.* **1994**, *101*, 5604.
(38) McCaffery, A. J. *Phys. Chem. Chem. Phys.* **2004**, *6*, 1637.
(39) McCaffery, A. J.; Pritchard, M.; Reisler, H. *J. Phys. Chem. A* **2010**, *114*, 2983and references therein.